Baroclinic instability within the ocean surface boundary layer

Christian E. Buckingham*

University of Southampton, Southampton, UK

Zammath Khaleel†

University of Southampton, Southampton, UK

Ayah Lazar

California Institute of Technology, Pasadena, California, USA

Adrian Martin

National Oceanography Centre, Southampton, UK

John Allen

University of Portsmouth, Portsmouth, UK

Alberto Naveira Garabato

University of Southampton, Southampton, UK

Corresponding author address: Christian E. Buckingham, University of Southampton, National

Oceanography Centre, European Way, Southampton, Hampshire, SO14 3ZH, United Kingdom

E-mail: c.e.buckingham@soton.ac.uk

†Current affiliation: Ministry of Environment and Energy, Malé, Maldives

ABSTRACT

A single satellite image of an ocean front coincident with *in situ* measurements of density from a towed, profiling instrument is examined for evidence of submesoscale baroclinic instability (BCI). The image was taken on 19 September 2012 at 03:34 UTC by the Visible and Infrared Imaging Radiometer Suite (VIIRS) on the Suomi/NPP spacecraft and consists of brightness temperatures collected within the infrared band at 390-m pixel resolution over the extratropical North Atlantic. The ocean front (i) is characterized by a 0.5–0.7°C change in temperature over a 10–25-km distance, (ii) results from the convergence of cool/warm water masses by the mesoscale eddy field, and (iii) is populated by several submesoscale vortices, or eddies, along the frontal boundary. While horizontal shear is one mechanism for generating submesoscale eddies (*Munk et al.*, 2000), here we consider an alternative hypothesis: that observed eddies are the result of BCI within the ocean surface boundary layer (SBL; *Eldevik and Dysthe*, 2002). Vertical and lateral buoyancy gradients, as well as SBL thickness, are estimated from *in situ* measurements. Theoretical eddy sizes corresponding to the most unstable mode of an Eady model are then computed and compared with observed eddy sizes. Sensitivities to model parameters are discussed. In most cases, we find good agreement between predicted and observed eddy sizes. Growth rates were not estimated due to severe cloud cover before and after the event. Given observed Rossby numbers are small, BCI provides a plausible explanation for the observed submesoscale eddies, with wider application to open-ocean conditions where shear is small.

1. Introduction

Studies have recently identified submesoscale processes as important in controlling stratification, dissipation, mixing and primary productivity within the upper ocean (Haine and Marshall 1998; Molemaker et al. 2005; Müller et al. 2005; Boccaletti et al. 2007; Fox-Kemper et al. 2008; Fox-Kemper et al. 2008; Thomas et al. 2008; Belcher et al. 2012; Brüggemann and Eden 2015; Smith et al. 2016; Klein and Lapeyre 2009; Mahadevan et al. 2012; Lévy et al. 2012; Omand et al. 2015). As such, they represent an important component of Earth's climate system.

Climate-scale ocean models do not presently resolve the submesoscale. The horizontal scale associated with submesoscale motions in the surface boundary layer (SBL) is governed by the *local* radius of deformation, $R_d = NH/f$ (Thomas et al. 2008). Here, f is the Coriolis parameter, N is stratification and H is an effective depth of this boundary layer. A typical wintertime value at midlatitudes is $R_d = 4$ km, while during summer it is closer to 1 km. The time scale over which these phenomena evolve is the inertial period, $2\pi/f$, which is approximately 17 hours at midlatitudes. Sampling at high spatial and temporal resolutions is therefore necessary to capture such phenomena within ocean models. While these requirements limit model simulations due to computational demand, these same sampling requirements limit observations: submesoscale features are unresolved by traditional hydrographic measurement techniques. One avenue forward lies in the use of remotely sensed observations that capture the submesoscale in a single image.

Recent advances in satellite remote sensing have allowed scientists and engineers to better resolve the submesoscale. The Visible and Infrared Imaging Radiometer Suite (VIIRS) aboard the Suomi/National Polar-orbiting Partnership (NPP) provides ocean surface measurements approximately once or twice per day at nearly 390-m pixel resolution[1]. And this, from an instrument

---

[1]Brightness temperature is estimated at 390-m resolution, while sea surface temperature (SST) is estimated by combining brightness temperatures of neighboring pixels, resulting in a resolution of approximately 780 m.

orbiting at an altitude of 824 km. While admittedly limited by cloud cover, such sensors have the potential to support or disprove current theories regarding the role of submesoscale phenomena in Earth's climate and to lead to new discoveries.

Here, we demonstrate the utility of the VIIRS sensor for the study of submesoscale phenomena. By examining a single satellite image coincident with *in situ* measurements of an ocean front, we demonstrate that baroclinic instability (BCI) of the SBL provides a plausible explanation for the existence of submesoscale eddies observed along the frontal boundary. Note: horizontal shear can also generate submesoscale eddies (Flament et al. 1985; Munk et al. 2000) and likely plays a role, here. However, this generally requires large Rossby numbers and we do not observe such magnitudes. In conclusion, this study (a) demonstrates the benefit of high-resolution infrared imagery and (b) provides rare observational support for BCI in the open ocean.

An outline of the paper is as follows. In section 2, we describe the mesoscale context of the observations using satellite altimetry. We then introduce the high-resolution satellite image and depict the lateral and vertical structure of the front from hydrographic measurements. In section 3, we demonstrate that the observed front meets the condition for BCI and, in section 4, introduce the Eady model of BCI (Eady 1949). From this model, we estimate the fastest growing mode and, in section 5, compare observed eddy diameters with those predicted by the model. We close the study with a discussion (section 6) and conclusions (section 7).

2. Observations of an unstable ocean front

a. High-resolution satellite imagery

Figure 1a displays a synoptic-scale image of SSH and associated surface geostrophic currents valid 19 September 2012. Figure 1b displays nighttime temperatures measured by the VIIRS

4

sensor this same day. Figure 1c expands a portion of this image in the vicinity of an unstable front. Cyclonic circulation to the north and anticyclonic circulation to the south associated with these two mesoscale eddies causes a convergence of near-surface waters. In particular, cool waters are advected from the northwest and warm waters are advected from the southwest and, owing to their close proximity and strong strain field, this results in the observed front. Notable along the frontal boundary are several submesoscale vortices, or eddies, four of which are *wispy* in appearance. The appearance of these wisps is suggestive of the formation of *spiral* submesoscale eddies by an unstable flow, with warm waters advected in a predominantly cyclonic direction (Munk et al. 2000; Eldevik and Dysthe 2002).

b. Coincident hydrographic and current measurements

Coincident hydrographic measurements were made across the front during 19–21 September using a towed, profiling conductivity-temperature-depth (CTD) package (Pollard 1986).[2] This ship track is shown in Figure 1c. The instrument, referred to as SeaSoar II (specifications available at http://www.chelsea.co.uk/allproduct/marine/towed-vehicles/seasoar), was towed behind a ship and its angle-of-attack varied to characterize the front. Temperature, salinity and pressure within the upper 500 m were converted to potential density and mapped to an evenly-spaced grid using a Barnes analysis (Barnes 1964, 1994a,b,c). The horizontal smoothing scale was chosen so as to eliminate discontinuities between neighboring SeaSoar tracks; we selected an isotropic 10-km smoothing scale, approximately three times the deformation radius. The resulting fields were smoothed vertically using a scale of 5 dbar.

Absolute velocity was also estimated using the geostrophic method (Pond and Pickard 1983). We computed dynamic height from the density field, estimated geostrophic velocities and refer-

---

[2]This was entirely by chance, and demonstrates the usefulness of aerial coverage during a field campaign.

5

enced these velocities to those measured at depth measured by a 75-kHz ship-mounted acoustic

Doppler current profiler (ADCP) (Pollard and Regier 1992). By comparing ADCP absolute ve-

locity profiles with geostrophic shear estimated from the SeaSoar survey, the best match in shape

was obtained at 329 m and deeper. Hence, we used a reference depth of 330 m when calculating

absolute geostrophic velocities. In summary, we have three-dimensional (3D) density and velocity

fields sufficient to characterize the structure of the front.

Figure 2a illustrates cross-sections of potential density, ρ_θ, in the vicinity of the front; Figure

2b depicts an along-front average of potential density, $\overline{\rho}_\theta$; and Figure 2c illustrates an along-front

average of the down-front geostrophic velocity, $\overline{u}$. The existence of a lateral density gradient in

Figures 2a and 2b demonstrates that sharp changes in temperature evident from the satellite image

are *not* compensated by changes in salinity (Rudnick and Ferrari 1999); that is, the front is baro-

clinic. Also, this gradient is greatest in the surface layer at depths $|z| < 50$ m. Finally, Figure 2c

reveals that the magnitude of horizontal flow is 30 cm s^{-1}, with a considerable fraction attributed

to the deeper mesoscale eddy field. [The maximum flow $\overline{u}$ associated with the submesoscale front

is approximately 5 cm s^{-1} (not shown).] In summary, both altimeter-derived sea surface height

and hydrographic observations support the prototypical view of an ocean front intensified by the

confluence of surface waters by mesoscale stirring.

3. Condition for instability

A necessary but insufficient criterion for BCI is that the gradient of background potential vor-

ticity (PV), $\partial\overline{q}/\partial y$, change sign within the flow (Charney and Stern 1962; Eliassen 1983). Here,

$q = \omega_\mathbf{a} \cdot \nabla b$ is PV (Ertel 1942), $\omega_\mathbf{a} = 2\Omega + \nabla \times \mathbf{u}$ is absolute vorticity, 2Ω is Earth's vorticity vec-

tor, $\mathbf{u} = (u, v, w)$ is fluid velocity, $b = -g\rho_\theta/\rho_o$ is buoyancy, g is gravity, ρ_o is a reference density

(e.g., 1025 kg m^{-3}) and y is cross-front distance, increasing in the direction of dense water. Below,

6

we investigate whether the front satisfies this criteria, estimating q and $\overline{q}$ from objectively mapped fields, where the overbar denotes an along-front average.

It is helpful to quantify the degree to which the flow is horizontally sheared. We estimated the magnitude of shear from the gradient Rossby number, ζ/f, where $\zeta = (\nabla \times \mathbf{u}) \cdot \hat{\mathbf{z}}$ is the vertical component of relative vorticity. We found $|\mathrm{Ro}| < 0.45$ at all points in the flow. An along-front average depicts smaller values: $|\mathrm{Ro}| \approx |-(\partial \overline{u}/\partial y)/f| < 0.15$ (Figure 2d). Thus, while shear is present at the front, its magnitude is insufficient to overcome planetary rotation. These values are much smaller than those used by Munk et al. (2000) in their study of horizontally-sheared flows.

We next estimated the cross-frontal gradient of potential vorticity. Figure 2e illustrates $\partial \overline{q}/\partial y$ and contains two features of interest: (1) a pronounced vertical gradient and change in sign of $\partial \overline{q}/\partial y$ at depths 40–45 m and (2) a change in the sign of $\partial \overline{q}/\partial y$ at the front axis at depths 30–40 m. The first feature indicates that there is very little or no flow across the pycnocline. Fluid above the pycnocline is stretched vertically (i.e., decreased stratification) with increasing cross-front distance, so $\partial \overline{q}/\partial y < 0$. Conversely, by continuity, fluid in the deeper layer is stretched vertically with increasing cross-front distance, so that $\partial \overline{q}/\partial y > 0$. The second feature indicates that the observed front meets the criterion for baroclinic instability. That contours of $\partial \overline{q}/\partial y = 0$ are not entirely along isopycnals indicates relative vorticity plays a role in the sign-reversal. This is not surprising since realistic fronts are associated with horizontal shear (Eliassen 1983).

Motivated by the existence of a baroclinic front with Rossby numbers less than unity, and having established that the background PV gradient changes sign, we next consider the linear BCI problem.

7

4. Baroclinic instability within the SBL

BCI occurs when a density front is perturbed from its mean state. Owing to cross-front displacements of fluid, corresponding compression and stretching of the water column and, finally, its effect upon relative vorticity, the front is unstable to small-amplitude, low-frequency perturbations (Charney 1947; Eady 1949; Charney and Stern 1962). Of particular note, the front can be shown to be most unstable to disturbances characterized by a single wavelength. Below, we use a simple baroclinic frontal model, in combination with the *in situ* estimates of density, to estimate the horizontal scale of disturbances corresponding to this most unstable mode. We then compare observed eddy sizes with those predicted by this model.

a. The Eady model

The frontal model presented here is essentially that described by Eady (1949) but complete descriptions can be found in Pedlosky (1987); Cushman-Roisin (1994) and Kundu and Cohen (2008), among others. The model consists of a front in thermal wind balance (i.e., geostrophic and hydrostatic) with mean flow, U, directed in the positive x direction. Superimposed on this mean flow are perturbations with infinitesimal amplitude, $u' \ll U$. We also make the following simplifications:

1. the flow is inviscid

2. the horizontal scale of the front is small so that the Coriolis parameter, f, is constant

3. the boundary layer thickness, H, is constant

4. the vertical stratification, $N^2 = \partial b / \partial z$, is constant

5. the lateral stratification, $M^2 = -\partial b / \partial y = f \partial U / \partial z$, is constant

8

172   6. the vertical velocity, w, is much smaller than the horizontal velocity, $\mathbf{u_h} = (u, v)$ at all times

173   7. the vertical velocity, w, at the bottom and top of the layer ($z = 0, H$) is exactly zero.

174 The assumption of constant M^2 implies a vertical shear independent of depth: $\partial U/\partial z = U_o/H$.

175 Also, note that $U(x, y, z) = U(z)$. Finally, the statement that $w \ll u, v$ allows us to neglect vertical

176 velocity in the mean but it is essential in the perturbation state (i.e., $w = w'$). The assumption that

177 $w = 0$ at the bottom boundary is discussed in section 6.

178   We now outline the derivation of the most unstable mode. By (i) taking the curl of the horizontal

179 momentum equations, (ii) employing continuity, (iii) introducing mean and perturbation notation

180 into this expression (i.e., $u = U + u'$) and (iv) neglecting products of perturbations, one obtains

181 a linearized vortex stretching equation: $\partial \zeta'/\partial t + U \partial \zeta'/\partial x - f \partial w'/\partial z = 0$. Here, $\zeta' = \partial v/\partial x -$

182 $\partial u/\partial y$ is the vertical component of perturbation relative vorticity. This expression can further

183 be simplified into an equation of a single variable (e.g., pressure, p') by assuming perturbations

184 are approximately geostrophic and that density is conserved.[3] Expressing vorticity in terms of

185 pressure, $\zeta' = \nabla_h^2 p'/(f\rho_o)$, solving the density equation for $w = w'$, and substituting into the

186 stretching equation leads to the following:

$$\left(\frac{\partial}{\partial t} + U \frac{\partial}{\partial x} \right) \left[\nabla_h^2 p' + \frac{f^2}{N^2} \left(\frac{\partial^2 p'}{\partial z^2} \right) \right] = 0, \tag{1}$$

187 where we have neglected the meridional gradient of Coriolis owing to the scale of the problem.

188 Equation 1 governs the evolution of perturbations from a mean, thermal-wind state. As it is linear,

189 it is valid only at the onset of instability; it becomes increasingly inaccurate with time.

190   We first define a solution of the form $p' = \hat{p}(z)e^{i(kx+ly-\omega t)}$, where $\omega = \omega_r + i\omega_i$ is the complex

191 growth rate and k and l are real-valued, along- and cross-front wavenumbers. Introducing this into

---

[3]Again, the geostrophic approximation is discussed in section 6. Also, we express the vorticity equation in terms of pressure but equivalently

express this in terms of a horizontal streamfunction (Cushman-Roisin 1994).

Equation 1, we obtain an eigenvalue problem in terms of pressure:

$$\frac{\partial^2 \hat{p}}{\partial z^2} - \alpha^2 \hat{p} = 0, \tag{2}$$

where $\alpha^2 = N^2(k^2 + l^2)/f^2$ is the square of a scaled horizontal wavenumber. Equation 2 has the general solution $\hat{p} = A_1 e^{\alpha z} + A_2 e^{-\alpha z}$, where coefficients A_1 and A_2 are determined from boundary conditions. For non-trivial solutions, this yields an expression for the growth rate as a function of horizontal wavenumber:

$$\omega = \frac{kU_o}{2} \pm f \left[\frac{1}{\text{Ri}} \left(\frac{\alpha H}{2} - \tanh \frac{\alpha H}{2} \right) \left(\frac{\alpha H}{2} - \coth \frac{\alpha H}{2} \right) \right]^{1/2}, \tag{3}$$

where $\text{Ri} = N^2 H^2 / U_o^2 = f^2 N^2 / M^4$ is the balanced gradient Richardson number. Without loss of generality, we let $l = 0$ so that $\alpha = (N/f)|k|$. Given perturbations of the form $p' \sim e^{-i\omega t}$, disturbances will grow unbounded if the imaginary part of ω is positive. This requires the quantity inside brackets be negative, and occurs for $\alpha H < 2.4$, demonstrating that the front is unstable to low-wavenumber perturbations. The fastest growing mode has wavelength $\lambda_{max} = 2\pi/|k| \approx 3.9 R_d$ (Pedlosky 1987; Cushman-Roisin 1994; Kundu and Cohen 2008).

Strictly speaking, the above expression is valid only for $\text{Ri} \gg 1$. Stone (1966) derived an expression for the growth rate under conditions of low Ri. While we do not observe such low values of the balanced gradient Richardson number (i.e., $10 < \text{Ri} < 75$ at all points in the flow), we nevertheless compared Stone's approximation with the imaginary part of Equation 3 and found they yield identical growth rates and wavelengths for the most unstable mode.

b. Growth rates from hydrographic data

The appearance of vortices on the frontal boundary suggests the front is actively undergoing instability. Therefore, the growth rates should be well represented by Equation 3. Relevant ocean parameters were estimated from hydrographic measurements, including SBL thickness, H, verti-

cal stratification, N/f, and lateral stratification, M/f. Motivated by the lack of flow across the pycnocline as revealed by $\partial \overline{q}/\partial y$ (cf. section 3, SBL thickness was defined as the average depth of the pycnocline. It effectively models the ocean as a two-layer fluid. We estimated H as the average depth of peak stratification, obtaining a value $\mu_H = 43$ m. We also retained information on the standard deviation of these depths: $\sigma_H = 5$ m. Stratifications within the SBL were computed as average values above this depth, yielding $\mu_{N/f} = 90$ and $\mu_{M/f} = 2.5$. Because variations in N/f and M/f are largely determined by changes in H, we also computed characteristic values of N/f and M/f for additional layer thicknesses, corresponding to $\mu_H \pm \sigma_H$. In summary, we obtained estimates of N/f and M/f for $H_1 = 38$, $H_2 = 43$ and $H_3 = 48$ m (Figure 3a).

Figure 3b depicts growth rates for the observed values of H, N/f and M/f, with the most unstable modes highlighted by red asterisks. The gray region in Figure 3b reflects our uncertainty in the corresponding wavelengths given uncertainty in H.

While mixed layer depth (MLD) is not the relevant depth scale for this problem, it is nonetheless interesting to observe how growth rates compare when using MLD for the depth of the SBL. Here, MLD has been defined as the depth at which potential density exceeds that observed at 15 m by an amount of 0.01 kg m^{-3} (de Boyer Montégut et al. 2004), and yields an average value of 24 m. We display in Figure 3a the growth rates corresponding to this depth, H_4. This yields higher growth rates but considerably smaller wavelengths.

5. Comparison of predicted and observed eddy sizes

Predictions of eddy size follow directly from the model presented above: eddy diameters are estimated at one-half the wavelength of the most unstable mode. This can be rationalized by observing that a sinusoidal pressure (or temperature) disturbance can be considered as two neighboring anomalies of equal amplitude but opposite sign. Observed eddy sizes were estimated from

11

the satellite image in three ways (Appendix). The rationale for computing these in different ways is that we have little knowledge of the best method for estimating the sizes of such features and spread in our estimates provides a measure of observation uncertainty. Illustrations of each method applied to the satellite image are shown in Figure 4 and the comparisons of predicted and observed eddy diameters is summarized in Table 1. We also highlight, in Figure 3b, observed eddy diameters using vertical black arrows to help compare predicted and observed eddy scales. Given uncertainty in the wavelength of the most unstable mode derived from hydrographic measurements, we find good agreement between predicted and observed eddy diameters under linear BCI.

6. Discussion

While the analytical model of Eady is attractive owing to its simplicity, it has several limitations. We expect nonlinearities not considered in this model will tend to broaden the scale of disturbances when compared to those predicted owing to an inverse energy cascade. An additional simplification includes the assumption that $w' = 0$ at the bottom boundary. Boccaletti et al. (2007) investigated the use of a non-zero vertical velocity at the bottom boundary, where interface displacements due to internal waves and lateral gradients in pycnocline. The main findings of their study are (a) a small portion of energy goes into the maintenance of interfacial waves and (b) negative cross-front gradients in pycnocline depth, $\partial H / \partial y < 0$, act to stabilize the front, shifting the fastest growing mode to larger wavenumbers (shorter wavelengths). This implies a reduction in the size of predicted submesoscale vortices, which would make them closer to the observations. Finally, the approximation that perturbations are geostrophic may not be valid. Grooms (2015) investigated the extent to which curvature modifies the linear Eady model. He finds that, while results are for the most part unchanged, ageostrophic curvature effects introduce an asymmetry in the scale of the most unstable mode. While such an asymmetry is not observed in our satel-

12

lite image, we nevertheless acknowledge its importance for understanding the exchange of energy between the front and perturbations, with implications for energy transfer between scales (Müller et al. 2005; Brüggemann and Eden 2015).

From an observational viewpoint, the SeaSoar and ADCP survey is limiting, as well. First, it is likely that the hydrographic survey sampled in a re-stratified area, as the eddies have already developed. In this case, N/f would be reduced and would result in predicted eddy sizes smaller than those reported here. Second, the horizontal smoothing scale of the objectively mapped fields is 10 km. Therefore, in an effort to eliminate discontinuities between SeaSoar tracks, it is possible that lateral gradients may have been reduced too much. A consequence is that growth rates and Rossby numbers reported here are reduced relative to their true values.

It is interesting that using the MLD for the thickness of the SBL yields predicted eddy sizes much smaller than observed eddy sizes. This discrepancy between terminology and underlying physics leads us to suggest that "baroclinic instability within the SBL" may be a more apt phrase than "mixed layer instability" in describing the BCI process.

What is the primary energy source for the disturbance?

BTI is a horizontal shear instability that derives its energy from kinetic energy in the flow. In contrast, BCI derives its energy from the potential energy of the flow. While the production of sub-mesoscale vortices results from both (Munk et al. 2000; Eldevik and Dysthe 2002), distinguishing between BTI and BCI is important for understanding how energy is fluxed from the mesoscale to the submesoscale. Thus, while this brief observational study has focused on BCI as a mechanism for generating such vortices, it is likely that horizontal shear plays a role (cf. section 3). One method of quantifying their relative contributions is through analysis of realistic numerical simulations. We leave this as an exercise for a future study.

13

7. Conclusions

There is an obvious need for improved strategies for observing submesoscale flows. In this study, we have demonstrated the utility of infrared satellite imagery in providing valuable information at the submesoscale. A single snapshot of the ocean surface coincident with *in situ* hydrographic measurements has enabled a straightforward comparison of observed and theoretically predicted eddy diameters. We found that observed eddy diameters are approximately equal to those predicted by the linear instability model of Eady (1949). While observed growth rates could be estimated due to severe cloud cover before and after the image, these observations nevertheless demonstrate that BCI is a plausible explanation for the observed submesoscale vortices in the ocean. This may find wider application in the open ocean, where the Rossby number is small.

One of the more interesting aspects of this brief study is the manner in which the observed front relates to the larger, mesoscale flow field. Indeed, the combination of infrared satellite imagery, altimeter-derived surface currents and hydrographic measurements all depict frontogenesis forced by the mesoscale flow. A lateral density gradient in the open ocean is intensified by the convergence of cool, northern and warm, southern waters by the mesoscale eddy field. This front then becomes unstable to low-wavenumber perturbations and, through a combination of cross-frontal displacement and vortex stretching, extracts potential energy from the mesoscale eddy field in the form of submesoscale vortices. Thus, in addition to demonstrating the formation of submesoscale eddies in the ocean, this brief study has provided observational support for energy exchange between mesoscale and submesoscale phenomena.

14

APPENDIX

Estimating observed eddy sizes

Observed eddy sizes were estimated from the satellite image in three ways. In methods methods 1 and 2, we estimated eddy diameters as half the wavelengths of peak power. In method 3, the eddy diameter was estimated as twice the most probable radius of curvature. Below, we outline each method.

a. Method 1: spectra of temperature

In the first method, we identified the peak in the power spectral density (PSD) of temperature obtained along transects of the front. The PSD was computed using both traditional and parametric spectral estimation approaches. The former uses the method of averaged, modified periodograms (Welch 1967; Harris 1978), while the latter models observations as the result of an autoregressive (AR) discrete-time process with $n = 25$ degrees of freedom (Yule 1927; Walker 1931). The advantage of the AR approach is that wavenumber resolution does not depend upon the length of the record (Kay and Marple 1981).

15

b. Method 2: spectra of the frontal boundary

In the second method, we identified the peak in the PSD of displacements of the frontal boundary, again, using both spectral approaches. In order to isolate the frontal boundary, we used a population-based front detection algorithm (Cayula and Cornillon 1992; Buckingham et al. 2014). The histogram portion of this algorithm operates by identifying two populations from the distribution of temperature; surface temperatures categorized as falling within cool and warm populations were identified. The resulting binary image was then processed using morphological operations (Gonzalez et al. 2004) and the boundary separating the two temperature populations was identified.

c. Method 3: radius of curvature

In the third method, we estimated the radius of curvature of the frontal boundary and identified its most frequently occurring value. The radius of curvature is given by $R = |1/\kappa|$, where

$$\kappa = \frac{\dot{x}\ddot{y} - \dot{y}\ddot{x}}{(\dot{x}^2 + \dot{y}^2)^{3/2}} \tag{A1}$$

is the curvature, and $\dot{x}$, $\dot{y}$, $\ddot{x}$ and $\ddot{y}$ denote first and second derivatives of zonal and meridional displacements with respect to distance along the boundary, s (e.g., $\dot{x} = dx/ds$). This expression was evaluated in its discrete form using first and second differences. We then identified the most probable value of R. While this was done using both a histogram and a PDF-fit to the observed radii. The fit reduces the dependence on bin size when estimating this value from a histogram.[4]

---

[4]The radius, $R = (x^2 + y^2)^{1/2}$, follows a Rayleigh distribution if zonal and meridional boundary displacements of the frontal boundary, x and y, are normally distributed random variables. We used the Weibull distribution, which is a generalization of the Rayleigh distribution that handles non-normally distributed random variables.

References

Barnes, S. L., 1964: A technique for maximizing details in numerical weather map analysis. *Journal of Applied Meteorology*, **3 (4)**, 396–409, doi:10.1175/1520-0450(1964)003⟨0396: ATFMDI⟩2.0.CO;2.

Barnes, S. L., 1994a: Applications of the Barnes objective analysis scheme. Part I: Effects of under sampling, wave position, and station randomness. *Journal of Atmospheric and Oceanic Technology*, **11 (6)**, 1433–1448.

Barnes, S. L., 1994b: Applications of the Barnes objective analysis scheme. Part II: Improving derivative estimates. *Journal of Atmospheric and Oceanic Technology*, **11 (6)**, 1449–1458.

Barnes, S. L., 1994c: Applications of the Barnes objective analysis scheme. Part III: Tuning for minimum error. *Journal of Atmospheric and Oceanic Technology*, **11 (6)**, 1459–1479.

Belcher, S. E., and Coauthors, 2012: A global perspective on Langmuir turbulence in the ocean surface boundary layer. *Geophysical Research Letters*, **39 (18)**, n/a–n/a, doi:10.1029/ 2012GL052932, 118605.

Boccaletti, G., R. Ferrari, and B. Fox-Kemper, 2007: Mixed layer instabilities and restratification. *Journal of Physical Oceanography*, **37 (9)**, 2228–2250.

Brüggemann, N., and C. Eden, 2015: Routes to dissipation under different dynamical conditions. *Journal of Physical Oceanography*, **45 (8)**, 2149–2168, doi:10.1175/JPO-D-14-0205.1.

Buckingham, C. E., P. C. Cornillon, F. Schloesser, and K. M. Obenour, 2014: Global observations of quasi-zonal bands in microwave sea surface temperature. *Journal of Geophysical Research: Oceans*, **119 (8)**, 4840–4866, doi:10.1002/2014JC010088.

17

Cayula, J.-F., and P. Cornillon, 1992: Edge detection algorithm for SST images. *Journal of Atmo-spheric and Oceanic Technology*, **9 (1)**, 67–80.

Charney, J. G., 1947: The dynamics of long waves in a baroclinic westerly current. *Journal of Meteorology*, **4 (5)**, 136–162.

Charney, J. G., and M. E. Stern, 1962: On the stability of internal baroclinic jets in a rotating atmosphere. *Journal of the Atmospheric Sciences*, **19 (2)**, 159–172, doi:10.1175/1520-0469(1962)019⟨0159:OTSOIB⟩2.0.CO;2.

Cushman-Roisin, B., 1994: *Introduction to geophysical fluid dynamics*. Prentice Hall, Englewood Cliffs, N.J., includes bibliographical references (p. 303-312) and index.

de Boyer Montégut, C., G. Madec, A. S. Fischer, A. Lazar, and D. Iudicone, 2004: Mixed layer depth over the global ocean: An examination of profile data and a profile-based climatology. *Journal of Geophysical Research: Oceans*, **109 (C12)**, doi:10.1029/2004JC002378, c12003.

Eady, E. T., 1949: Long waves and cyclone waves. *Tellus A*, **1 (3)**.

Eldevik, T., and K. B. Dysthe, 2002: Spiral eddies. *Journal of Physical Oceanography*, **32 (3)**, 851–869, doi:10.1175/1520-0485(2002)032⟨0851:SE⟩2.0.CO;2.

Eliassen, A., 1983: The Charney-Stern theorem on barotropic-baroclinic instability. *pure and applied geophysics*, **121 (3)**, 563–572, doi:10.1007/BF02590155.

Ertel, H., 1942: Ein neuer hydrodynamischer wirbelsatz. *Meteorol. Z.*, **59**, 271–281.

Flament, P., L. Armi, and L. Washburn, 1985: The evolving structure of an upwelling filament. *Journal of Geophysical Research: Oceans*, **90 (C6)**, 11 765–11 778, doi:10.1029/JC090iC06p11765.

18

Fox-Kemper, B., G. Danabasoglu, R. Ferrari, and R. W. Hallberg, 2008: Parameterizing submesoscale physics in global climate models. *CLIVAR Exchanges*, **13 (1)**, 3–5.

Fox-Kemper, B., R. Ferrari, and R. Hallberg, 2008: Parameterization of mixed layer eddies. Part I: Theory and diagnosis. *Journal of Physical Oceanography*, **38 (6)**, 1145–1165.

Gonzalez, R. C., R. E. Woods, and S. L. Eddins, 2004: *Digital image processing using MATLAB*. Pearson Education India.

Grooms, I., 2015: Submesoscale baroclinic instability in the balance equations. *Journal of Fluid Mechanics*, **762**, 256–272.

Haine, T. W., and J. Marshall, 1998: Gravitational, symmetric, and baroclinic instability of the ocean mixed layer. *Journal of physical oceanography*, **28 (4)**, 634–658.

Harris, F. J., 1978: On the use of windows for harmonic analysis with the discrete fourier transform. *Proceedings of the IEEE*, **66 (1)**, 51–83.

Kay, S., and J. Marple, S.L., 1981: Spectrum analysis: a modern perspective. *Proceedings of the IEEE*, **69 (11)**, 1380–1419, doi:10.1109/PROC.1981.12184.

Klein, P., and G. Lapeyre, 2009: The oceanic vertical pump induced by mesoscale and submesoscale turbulence. *Annual Review of Marine Science*, **1 (1)**, 351–375, doi:10.1146/annurev. marine.010908.163704.

Kundu, P. K., and I. M. Cohen, 2008: *Fluid Mechanics*. 4th ed., Elsevier, Oxford, includes bibliographical references and index.

Lévy, M., R. Ferrari, P. J. S. Franks, A. P. Martin, and P. Rivière, 2012: Bringing physics to life at the submesoscale. *Geophysical Research Letters*, **39 (14)**, doi:10.1029/2012GL052756, 114602.

19

Mahadevan, A., E. D'Asaro, C. Lee, and M. J. Perry, 2012: Eddy-driven stratification initiates North Atlantic spring phytoplankton blooms. *Science*, **337 (6090)**, 54–58.

Molemaker, M. J., J. C. McWilliams, and I. Yavneh, 2005: Baroclinic instability and loss of balance. *J. Phys Oceanogr.*, **35**, 1505–1517.

Müller, P., J. McWilliams, and M. Molemaker, 2005: Routes to dissipation in the ocean: The 2D/3D turbulence conundrum. *Marine turbulence: theories, observations and models*, 397–405.

Munk, W., L. Armi, K. Fischer, and F. Zachariasen, 2000: Spirals on the sea. *Proceedings of the Royal Society of London A: Mathematical, Physical and Engineering Sciences*, The Royal Society, Vol. 456, 1217–1280.

Omand, M. M., E. A. D'Asaro, C. M. Lee, M. J. Perry, N. Briggs, I. Cetinić, and A. Mahadevan, 2015: Eddy-driven subduction exports particulate organic carbon from the spring bloom. *Science*, doi:10.1126/science.1260062.

Pedlosky, J., 1987: *Geophysical Fluid Dynamics*. 2nd ed., Springer-Verlag, Springer New York, New York, 1–710 pp.

Pollard, R., 1986: Frontal surveys with a towed profiling conductivity/temperature/depth measurement package (SeaSoar). *Nature*, **323 (6087)**, 433–435.

Pollard, R. T., and L. A. Regier, 1992: Vorticity and vertical circulation at an ocean front. *Journal of Physical Oceanography*, **22 (6)**, 609–625, doi:10.1175/1520-0485(1992)022⟨0609: VAVCAA⟩2.0.CO;2.

Pond, S., and G. L. Pickard, 1983: *Introductory Dynamical Oceanography*. 2nd ed., Butterworth-Heinemann, Oxford, 1 - 329 pp., doi:http://dx.doi.org/10.1016/B978-0-08-057054-9.50007-9.

Rudnick, D. L., and R. Ferrari, 1999: Compensation of horizontal temperature and salinity gradients in the ocean mixed layer. *Science*, **283 (5401)**, 526–529, doi:10.1126/science.283.5401.526.

Smith, K. M., P. E. Hamlington, and B. Fox-Kemper, 2016: Effects of submesoscale turbulence on ocean tracers. *Journal of Geophysical Research: Oceans*, doi:10.1002/2015JC011089.

Stone, P. H., 1966: On non-geostrophic baroclinic stability. *Journal of the Atmospheric Sciences*, **23 (4)**, 390–400.

Thomas, L. N., A. Tandon, and A. Mahadevan, 2008: Submesoscale processes and dynamics. *Ocean Modeling in an Eddying Regime, Geophys. Monogr. Ser*, **177**, 17–38.

Walker, G., 1931: On periodicity in series of related terms. *Proceedings of the Royal Society of London. Series A, Containing Papers of a Mathematical and Physical Character*, 518–532.

Welch, P. D., 1967: The use of fast fourier transform for the estimation of power spectra: A method based on time averaging over short, modified periodograms. *IEEE Transactions on audio and electroacoustics*, **15 (2)**, 70–73.

Yule, G. U., 1927: On a method of investigating periodicities in disturbed series, with special reference to wolfer's sunspot numbers. *Philosophical Transactions of the Royal Society of London. Series A, Containing Papers of a Mathematical or Physical Character*, 267–298.

LIST OF TABLES

TABLE 1. Predicted and observed eddy scales. Predicted eddy scales follow from the Eady model, while observed eddy scales were estimated using several methods (cf. Figure 4). Eddy diameters are defined as one-half the wavelength or twice the radius of curvature. Numbers in bold correspond to those estimates believed to be more accurate owing to improved wavenumber resolution in spectra.

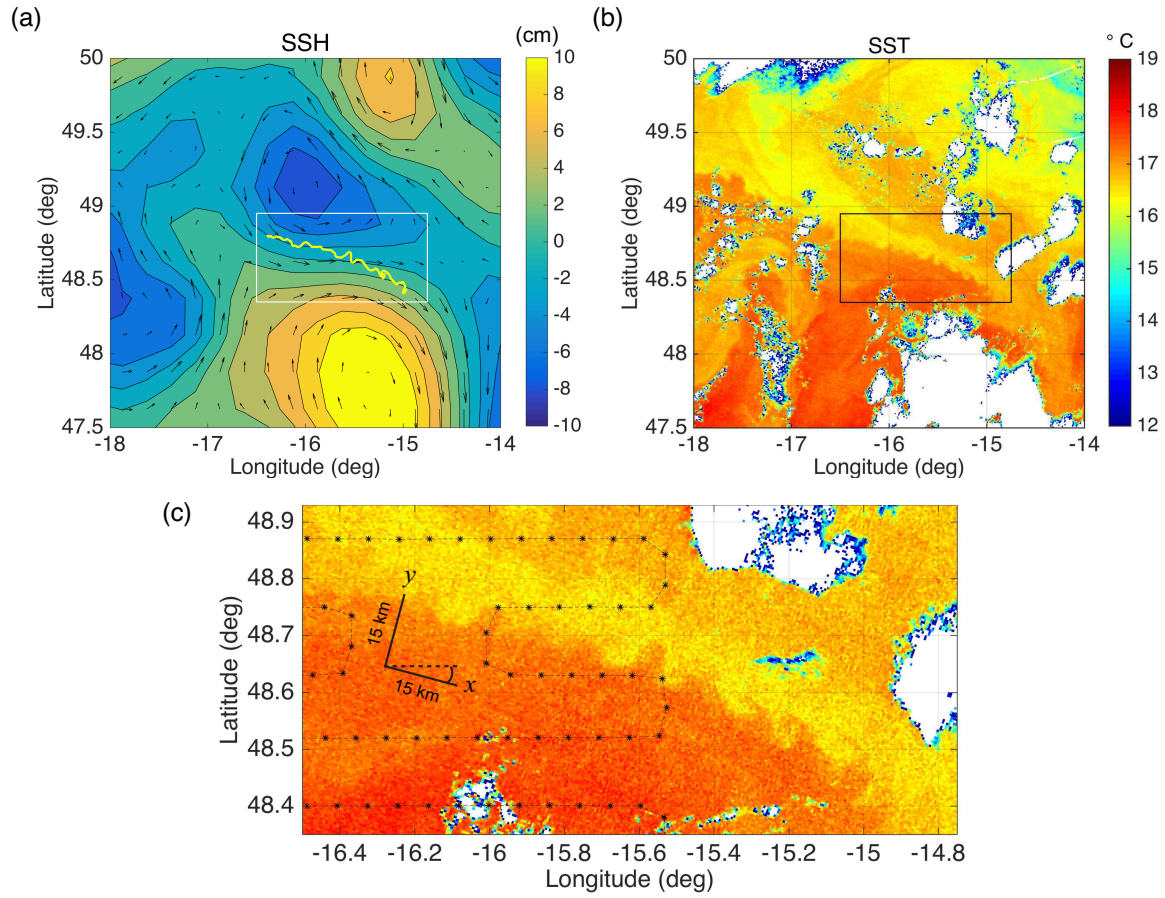| Type	Method	Wavelength (km)	Radius (km)	Diameter (km)
predicted	linear BCI model	10.8–19.6	–	5.4–9.8
observed	spectra of temperature	11.6, **13.0**	–	5.8, **6.5**
observed	spectra of frontal boundary	12.0, **13.5**	–	6.0, **6.8**
observed	radius of curvature	–	2.3-3.0, 2.6	5.2

24

FIG. 1. (a) Sea surface height (SSH) and geostrophic currents from satellite altimetry (valid 19 September 2012). (b) Sea surface temperature (SST) from the Visible and Infrared Imaging Radiometer Suite (VIIRS) onboard Suomi/NPP (valid 19 September 2012, 0334 UTC). (c) Same as Figure 1b but consisting of brightness temperatures magnified in the region of the unstable front. In (a), the yellow line corresponds to the identified front; in (b) and (c), white and neighboring cool pixels indicate cloud contamination; the thin line and dots in (c) denote ship track and hydrographic/ADCP measurements used in this study (19–21 September 2012).
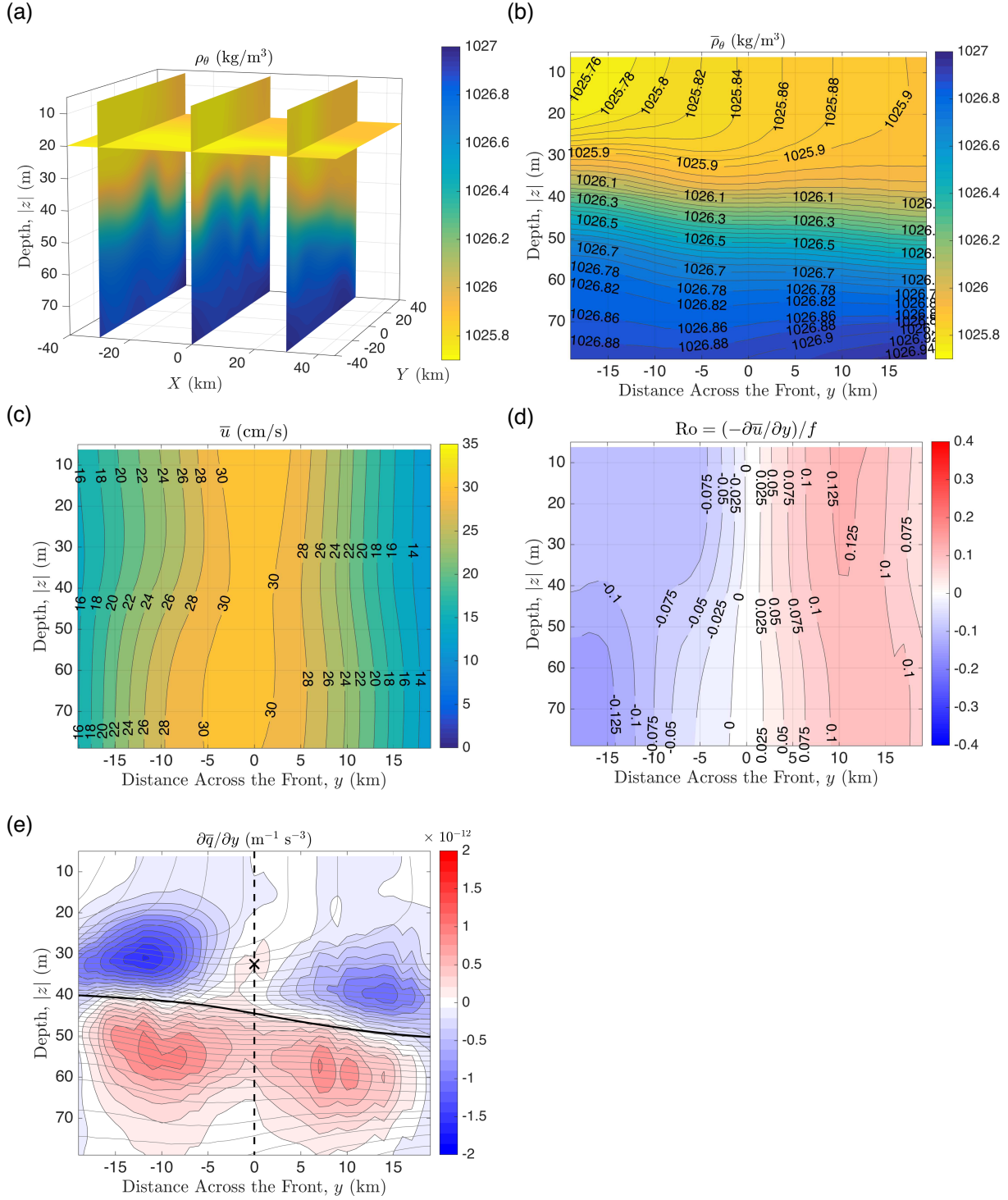
25

FIG. 2. (a) Vertical and horizontal cross-sections of potential density, ρ_θ, in the vicinity of the front; X and Y are distances in East and North directions, respectively; (b) composite of potential density, $\overline{\rho}_\theta$, generated by averaging values in a direction $\sim 15°$ clockwise of East (cf. Figure 1c); (c) composite of down-front velocity, $\overline{u}$; (d) horizontal gradient Rossby number, Ro $= \overline{\zeta}/f$; (e) cross-front gradient of background potential vorticity, $\partial\overline{q}/\partial y$. For reference, in (e) we overlay contours of constant potential density (thin gray) and peak stratification (solid black); the symbol (X) highlights a location discussed in the text (section 3).
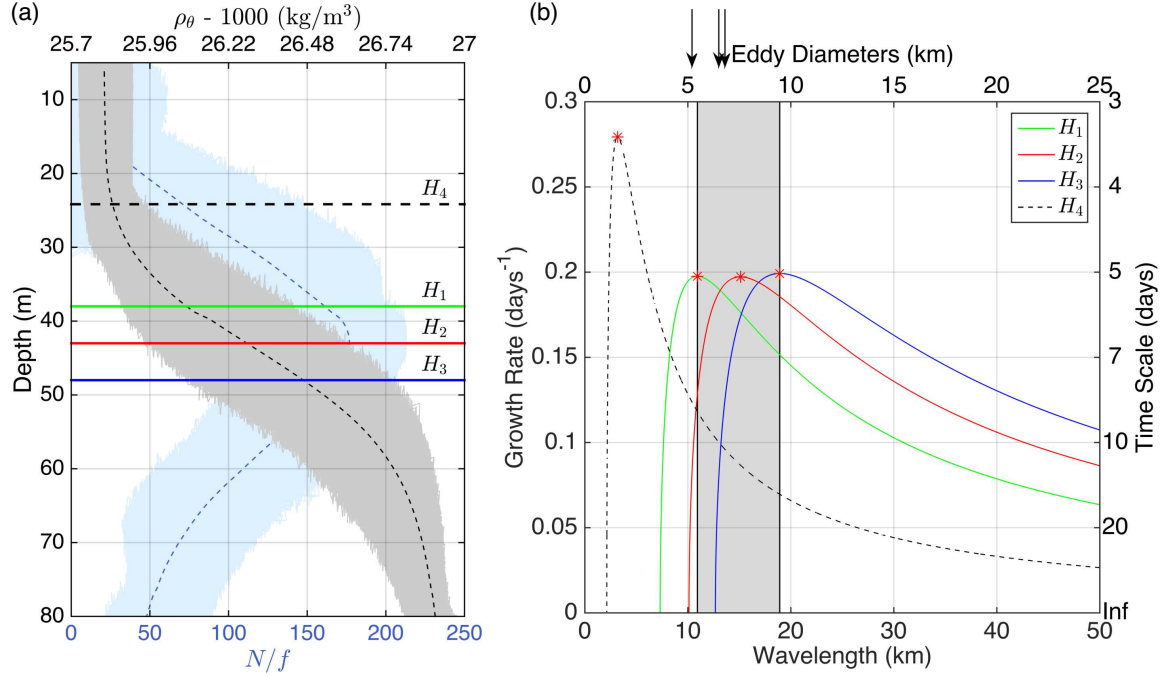
FIG. 3. (a) Potential density (gray) and buoyancy frequency (blue) near the front. (b) Growth rates as a function of horizontal scale from the Eady model. In (a), colored solid lines (H_1, H_2, H_3) indicate the average depth of peak stratification $\pm\sigma$, and is the definition of SBL thickness used in this paper. The horizontal dashed line (H_4) indicates the value obtained if defining SBL thickness from the MLD (de Boyer Montégut et al. 2004). In (b), we illustrate the growth rates corresponding to these definitions of SBL thickness, with corresponding changes in stratification and lateral density gradients. Note that H_2 represents our best estimate of SBL thickness, so that the shaded region denotes confidence in our estimate of the wavelength of the most unstable mode. Asterisks mark the wavelength of the most unstable mode and arrows highlight observed eddy diameters from the satellite image (cf. Table 1).
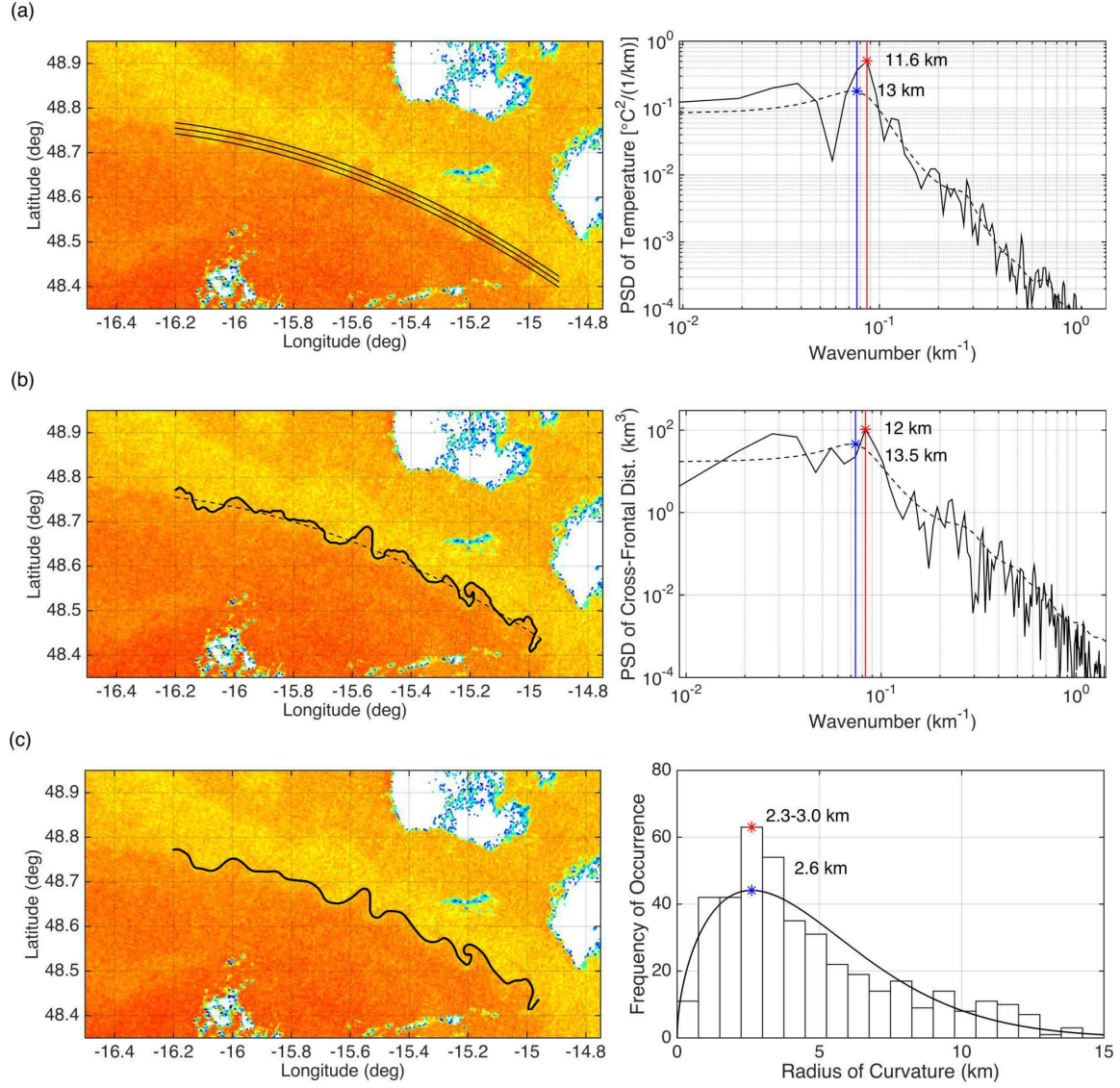
27

FIG. 4. Illustration of three methods used to estimate observed eddy diameters. In (a) and (b), we illustrate spectra computed using both traditional (solid) and parametric (dashed) spectral approaches. Asterisks highlight wavelengths corresponding to peaks in the spectral energy. In (c), we estimated the radius of curvature, $R = |1/\kappa|$, of the frontal boundary, where the boundary was smoothed slightly to improve estimates of curvature. Asterisks highlight the (red) most frequently occurring and (blue) probable radii given a Weibull fit to the data. Eddy diameters were estimated as (a,b) half the peak wavelength and (c) twice the most probable radius of curvature.